

Experimental measurement of local noise power spectrum (NPS) in photon counting detector-CT (PCD-CT) using a single data acquisition

Chengzhu Zhang¹ | Ke Li^{1,2} | Ran Zhang¹ | Guang-Hong Chen^{1,2}

¹Department of Medical Physics, University of Wisconsin School of Medicine and Public Health, Madison, Wisconsin, USA

²Department of Radiology, University of Wisconsin School of Medicine and Public Health, Madison, Wisconsin, USA

Correspondence

Guang-Hong Chen, Department of Medical Physics, School of Medicine and Public Health, University of Wisconsin—Madison, Madison, WI 53705, USA; Department of Radiology, School of Medicine and Public Health, University of Wisconsin—Madison, Madison, WI 53705, USA.

Email: gchen7@wisc.edu

Funding information

National Institute of Biomedical Imaging and Bioengineering, Grant/Award Numbers: R01EB034011, R01EB032474; National Heart, Lung, and Blood Institute, Grant/Award Number: R01HL153594; Wisconsin Alumni Research Foundation (WARF)

Abstract

Background: Accurate noise power spectra (NPS) measurement in clinical X-ray CT exams is challenging due to the need for repeated scans, which expose patients to high radiation risks. A reliable method for single CT acquisition NPS estimation is thus highly desirable.

Purpose: To develop a method for estimating local NPS from a single photon counting detector-CT (PCD-CT) acquisition.

Methods: A novel nearly statistical bias-free estimator was constructed from the raw counts data of PCD-CT scan to estimate the variance of sinogram projection data. An analytical algorithm is employed to reconstruct point-wise covariance $\text{cov}(\mathbf{x}_i, \mathbf{x}_j)$ between any two image pixel/voxel locations \mathbf{x}_i and \mathbf{x}_j . A Fourier transform is applied to obtain the desired point-wise NPS for any chosen location \mathbf{x}_i . The method was validated using experimental data acquired from a benchtop PCD-CT system with various physical phantoms, and the results were compared with the conventional local NPS measurement method using repeated scans and statistical ensemble averaging.

Results: The experimental results demonstrate that (1) the proposed method can achieve pointwise/local NPS measurement for a region of interest (ROI) located at any chosen position, accurately characterizing the NPS with spatial structures resulting from image content heterogeneity; (2) the local NPS measured using the proposed method show a higher precision in the measured NPS compared to the conventional measurement method; (3) spatial averaging of the local NPS yields the conventional NPS for a given local ROI.

Conclusion: A new method was developed to enable local NPS from a single PCD-CT acquisition.

KEYWORDS

local image quality, noise power spectrum, task-specific

1 | INTRODUCTION

A quantitative evaluation of the performance of two-dimensional (2D) x-ray projection or computed tomography imaging systems requires the measurement of the noise power spectrum (NPS)^{1–39} and modulation

transfer function (MTF).^{40–43} Information about the radiation dose efficiency of the system is provided by the NPS,^{2,3,9,15,32,35,39} while the ability of the imaging system to maintain the signal fidelity at different spatial frequencies is characterized by the MTF.^{40–43} The identification of bottlenecks in an imaging chain that affect

This is an open access article under the terms of the [Creative Commons Attribution-NonCommercial-NoDerivs](#) License, which permits use and distribution in any medium, provided the original work is properly cited, the use is non-commercial and no modifications or adaptations are made.

© 2024 The Authors. *Medical Physics* published by Wiley Periodicals LLC on behalf of American Association of Physicists in Medicine.

the imaging performance can be achieved by measuring the NPS and MTF. This knowledge can be utilized to optimize the imaging system for specific imaging tasks using appropriate quantitative image quality evaluation metrics.^{44–54}

In the relatively straightforward MTF measurement process, edge responses in both phantom and clinical patient studies are evaluated to extract point spread functions (PSF), and a Fourier transform is subsequently applied to obtain the desired MTF. This can be achieved in a single data acquisition, although the result might be noisy. On the other hand, the standard method for measuring NPS requires that measurements be repeated under identical acquisition conditions, generating an ensemble of images.^{23,24} The statistical sample mean is then taken over a region of interest (ROI) of the images to produce the NPS over the selected ROI. While no problems are posed for physical phantom studies due to the absence of radiation concerns, data acquisition time may be extended. In certain cases, approximations can be introduced to facilitate the NPS measurement for a uniform phantom or other phantoms with predominantly piece-wise image content. For these simple image objects, the statistical sample mean over a statistically independent and identical ensemble of samples can be replaced by the spatial average over small patches of uniform regions in the phantom. However, the validity of this method depends on the assumption of independence and identical distribution (i.i.d) over these small noise patches. Satisfying the i.i.d assumption in CT images is challenging because the noise distribution is spatially nonstationary and varies significantly even for uniform phantom and filtered back-projection (FBP).^{10,11,14,18} Consequently, to account for the spatial variations of NPS in a local region, it is essential that NPS be estimated over small ROIs at multiple sampled locations in the scanning field of view (FOV) to understand potential performance variations across the FOV.

Phantom studies are commonly utilized for providing an overall performance quantification for an imaging system. However, to achieve a quantitative understanding of the imaging performance of a clinical CT imaging system for a specific patient, both MTF and NPS must be measured from patient scans to study performance for a specific clinical task at a specific anatomical location. In other words, NPS measurements must be performed for all local regions in the FOV, and task-specific performance studies^{14,47–54} can be successfully carried out only if the local NPS is reliably estimated from patient scans without repeated measurements. However, a quantitative assessment of NPS in clinical exams is exceptionally challenging due to the following reasons: (1) repeated scans for patients cannot be performed because of patient safety concerns, and (2) the uniformity and homogeneity assumptions used in phantom studies are severely violated due to the substantial het-

erogeneity of patient anatomy. Consequently, an open scientific question remains regarding how local NPS measurements can be experimentally measured without repeated scans.

The aim of this study was to develop an innovative method for accurately measuring local NPS from a single PCD-CT data acquisition. In this new method, the measured raw count data are utilized for two purposes: (1) image reconstruction, in which the data undergo a logarithmic transform to generate line integral projection data, and (2) constructing a nearly statistical bias-free estimator [i.e., bias-free up to the order of $\mathcal{O}\left(\frac{1}{N^3}\right)$, where N is the photon count] of the variance for each log-transformed projection datum. Using the constructed variance estimator from a single CT acquisition, the covariance between any two image pixels/voxels is reconstructed using a closed-form analytical FBP reconstruction algorithm (i.e., a FBP reconstruction of the covariance instead of the image). Once the local covariance over a desired ROI is reconstructed, a Fourier transform is applied to generate the local NPS. Experimental phantom data acquired from an benchtop PCD-CT system were utilized to validate the proposed local and task-specific NPS measurement method.

2 | THEORETICAL METHOD

Once a CT data acquisition is performed, the measured raw detector counts are log-transformed to estimate the projection data p_m for tomographic image reconstruction:

$$\hat{p}_m = \log \frac{\bar{N}_{0m}}{N_m} \quad (m = 1, 2, \dots, M), \quad (1)$$

where \bar{N}_{0m} represents the mean raw counts from the corresponding air scan, and N_m denotes the raw detector counts at a given acquisition view angle and a detector element. Using the above line integral projection data, the CT image $\hat{I}(\vec{x})$ can be reconstructed using the FBP algorithm, which can be generically written as the following discrete sum (detailed derivations are presented in Appendix):

$$\hat{I}(\vec{x}) = \sum_{m=1}^M \lambda_m(\vec{x}) \hat{p}_m. \quad (2)$$

Coefficients λ_m are the weighting factors that account for the effects of the data filtering, interpolation, and back-projection. These coefficients collect contributions of the measured data from each detector element and view angle to the reconstruction of \hat{I} at each spatial location \vec{x} . λ_m are independent of the acquired photon counts N_m , which only appear in \hat{p}_m via Equation (1).

2.1 | Brief review: Standard NPS measurement method with repeated acquisitions

Suppose the same image object is scanned K times under identical acquisition conditions. Images are first reconstructed using the conventional FBP algorithm shown in Equation (2) for each of the repeated acquisitions. The sample mean image, $\bar{I}(\vec{x})$, is generated from these K reconstructed images

$$\bar{I}(\vec{x}) = \frac{1}{K} \sum_{k=1}^K I^{(k)}(\vec{x}), \quad (3)$$

and then subtracted from each reconstructed image to generate the noise-only images, denoted as $\Delta I^{(k)}(\vec{x})$, where $k = 1, 2 \dots, K$:

$$\Delta I^{(k)}(\vec{x}) = I^{(k)}(\vec{x}) - \bar{I}(\vec{x}). \quad (4)$$

From these noise-only images, NPS for a given ROI can be estimated as follows^{23,24}:

$$\widetilde{NPS}_K(k_x, k_y) = \frac{\Delta x \Delta y}{N_x N_y} \frac{1}{K} \sum_{k=1}^K \left| \text{DFT}_{2D}[\Delta I^{(k)}(\vec{x})] \right|^2, \quad (5)$$

where DFT_{2D} denotes two-dimensional (2D) discrete Fourier transform (DFT), Δx and Δy denote the physical dimensions of the reconstructed image pixel, while N_x and N_y are the number of pixels along x and y dimensions of the ROI, respectively. The above formula summarizes the estimation of the NPS for a local ROI when the data acquisitions are repeated K times under identical experimental conditions.

2.2 | From covariance to NPS

In PCD-CT, the measured detector counts N_m and the correspondingly projection data \hat{p}_m can be approximately considered to be statistically independent regarding m , since they are measured from detector elements and different view angles. Using this statistical independence property, it can be shown^{10,11,14} that the expected value, $E[\hat{I}(\vec{x})]$ and covariance of the reconstructed image, $\text{COV } \hat{I}(\vec{x}_i; \vec{x}_j)$, are given below:

$$E[\hat{I}(\vec{x})] = \sum_{m=1}^M \lambda_m(\vec{x}) E[\hat{p}_m]; \quad (6)$$

$$\text{COV } \hat{I}(\vec{x}_i; \vec{x}_j) = \sum_{m=1}^M \lambda_m(\vec{x}_i) \lambda_m(\vec{x}_j) \text{var}(\hat{p}_m), \quad (7)$$

where $E[\hat{p}_m]$ is the statistical expectation of the line integral data, and $\text{var}(\hat{p}_m)$ is the variance of the post-log projection data. These results are well-known, as found in literature.^{10,11,14} It says that one can reconstruct the covariance of the reconstructed PCD-CT images provided that the variance of the projection data, $\text{var}(\hat{p}_m)$, is known.

In this work, local NPS from the above image covariance matrix is defined as follows: a 2D DFT is applied to $\text{COV } \hat{I}(\vec{x}_i; \vec{x}_j)$ over an ROI centered at \vec{x}_i (pivotal point):

$$\text{NPS}(k_x, k_y; \vec{x}_i) = \Delta x \Delta y \left| \text{DFT}_{2D}[\text{COV } \hat{I}(\vec{x}_i; \vec{x}_j)] \right|. \quad (8)$$

Note that the 2D DFT is taken with respect to $\vec{x}_j - \vec{x}_i$, namely the relative distance to the chosen pivotal point \vec{x}_i . Any image pixel in an ROI can be used as the pivotal point \vec{x}_i to generate the local NPS centered at the pivotal point. As a result, Equation (8) quantifies the local NPS at the anchor point \vec{x}_i .

If one is only interested in the overall NPS for the selected ROI, a spatial average can be performed over these local NPS included in the ROI as follows:

$$\overline{NPS}_{\text{ROI}}(k_x, k_y) = \frac{1}{R} \sum_{\vec{x}_i \in \text{ROI}} \text{NPS}(k_x, k_y; \vec{x}_i), \quad (9)$$

where R denotes the number of pivotal points used in the average.

It is important to emphasize that the image covariance, the projection data variance, and local NPS in Equations (7) and (8) involve mathematical expectation operations. Although these operations are meaningful in theoretical derivations, they do not yet offer a method for the experimental measurement of local NPS since one cannot calculate mathematical expectations using sampled experimental data. To experimentally measure the local NPS, one must construct a statistical estimator, denoted as $\widehat{\text{var}}(\hat{p}_m)$, from the sampled experimental data for the true projection data variance, $\text{var}(\hat{p}_m)$. In the following section, we introduce a novel method to construct the statistical estimator $\widehat{\text{var}}(\hat{p}_m)$ from a single PCD-CT acquisition, thereby enabling local NPS measurement from a single PCD-CT acquisition.

2.3 | Statistical estimator of projection data variance from a single PCD-CT acquisition

In addition to the concept of local NPS defined in Equation (8), another key contribution of this paper is the development of the following statistical estimator of the PCD-CT projection variance requiring only a single PCD-CT acquisition:

$$\widehat{\text{var}}(\hat{p}_m) = \frac{1}{N_m}. \quad (10)$$

The above estimator obviates the need for repeated scanning a given image object. This new estimator has the following mathematical expectation value:

$$\text{E}[\widehat{\text{var}(\hat{p}_m)}] = \text{E}\left[\frac{1}{N_m}\right] = \frac{1}{\bar{N}_m} + \dots \quad (11)$$

Using this new statistical estimator of the projection variance, the image covariance $\text{COV}_{\vec{i}}(\vec{x}_i; \vec{x}_j)$ in Equation (7) can be reconstructed with a single PCD-CT data acquisition. Before we proceed, the following question must be addressed first: whether the proposed variance estimator in Equation (10) is a good approximation of the true variance $\text{var}(\hat{p}_m)$. This question can be readily answered using well-known properties^{14,55,56} of the Poisson-distributed photon counts: it has been shown that $\text{var}(\hat{p}_m)$ is related to \bar{N}_m by

$$\begin{aligned} \text{var}(\hat{p}_m) &= \text{var}\left(\ln \frac{\bar{N}_{0m}}{N_m}\right) \\ &= \frac{1}{\bar{N}_m} + \frac{3}{2\bar{N}_m^2} + \frac{43}{12\bar{N}_m^3} + O\left(\frac{1}{\bar{N}_m^4}\right), \end{aligned} \quad (12)$$

where $O(\frac{1}{\bar{N}_m^4})$ denotes higher-order terms.

By comparing Equations (11) and (12), up to the leading order, we have the following result:

$$\text{E}[\widehat{\text{var}(\hat{p}_m)}] \approx \text{var}(\hat{p}_m). \quad (13)$$

This result indicates that the proposed estimator in Equation (10) is indeed an approximation of $\text{var}(\hat{p}_m)$. This justifies the validity of the proposed new estimator in Equation (10) from a single PCD-CT data acquisition.

In practical scenarios where photon counts at a detector element exceed 10, the first-order approximation presented in Equation (10) is generally sufficient, as the bias from neglecting higher-order terms is <1%. However, at extremely low exposure levels, the photon count at a detector element can be in single digits, rendering this leading-order approximation potentially inadequate. In such cases, it may be beneficial to include higher-order contributions and address potential zero counts, as recently demonstrated in CT number bias correction^{55–58} by our research group. These advanced methods can significantly reduce the statistical bias of the estimator, resulting in an estimator that is almost free of statistical bias. For convenience, we present an estimator that is bias-free up to the third order:

$$\widehat{\text{var}(\hat{p}_m)}^{\text{third-order}} = \frac{1}{N_m} + \frac{1}{2N_m^2} + \frac{1}{12N_m^3}. \quad (14)$$

Detailed derivations of this estimator is presented in the Appendix II to show that it is nearly bias-free up to the order of $\frac{1}{\bar{N}_m^4}$.

2.4 | Local NPS measurement from single PCD-CT acquisition

Using the estimator in Equation (7), PCD-CT image covariance can be estimated with a single PCD-CT acquisition:

$$\widehat{\text{COV}}_{\vec{i}}(\vec{x}_i, \vec{x}_j) \approx \sum_{m=1}^M \lambda_m(\vec{x}_i)\lambda_m(\vec{x}_j) \frac{1}{N_m}. \quad (15)$$

We would like to highlight a crucial difference between the new method in Equation (15) and the well-known method in Equation (7): instead of using \bar{N}_m , which cannot be known unless multiple repeated PCD-CT data acquisitions are performed, the proposed projection variance estimator uses N_m , enabling the PCD-CT image covariance and NPS to be estimated from a single data acquisition process.

In the case of $\vec{x}_i = \vec{x}_j$, the covariance estimator in Equation (15) becomes a new variance estimator for any image pixel/voxel at \vec{x}_i :

$$\widehat{\sigma}_{\vec{i}}^2(\vec{x}_i) \approx \sum_{m=1}^M \frac{1}{N_m} \lambda_m^2(\vec{x}_i), \quad (16)$$

This closed-form formula allows one to reconstruct the variance map from the raw counts data in parallel to the reconstruction of the PCD-CT image from the log-transformed sinogram data.

From $\widehat{\text{COV}}_{\vec{i}}(\vec{x}_i, \vec{x}_j)$ in Equation (15), the following 2D DFT can be taken over an ROI centered a pivotal point \vec{x}_i to experimentally measure the 2D NPS:

$$\widehat{\text{NPS}}(k_x, k_y; \vec{x}_i) = \Delta x \Delta y \left| \text{DFT}_{2D}[\widehat{\text{COV}}_{\vec{i}}(\vec{x}_i, \vec{x}_j)] \right| \quad (17)$$

Note that any image pixels within a target ROI can be used as the pivotal point in the above formula. Correspondingly, if one is only interested in the 2D NPS averaged over the target ROI, a spatial averaging of $\widehat{\text{NPS}}(k_x, k_y; \vec{x}_i)$ over \vec{x}_i can be performed as follows:

$$\widehat{\text{NPS}}_{\text{ROI}}(k_x, k_y) = \frac{1}{R} \sum_{\vec{x}_i \in \text{ROI}} \widehat{\text{NPS}}(k_x, k_y; \vec{x}_i), \quad (18)$$

Figure 1 summarizes the major differences between the conventional and proposed NPS estimation methods.

3 | EXPERIMENTAL VALIDATION METHOD

To experimentally validate the proposed local NPS measurement method using a single PCD-CT data

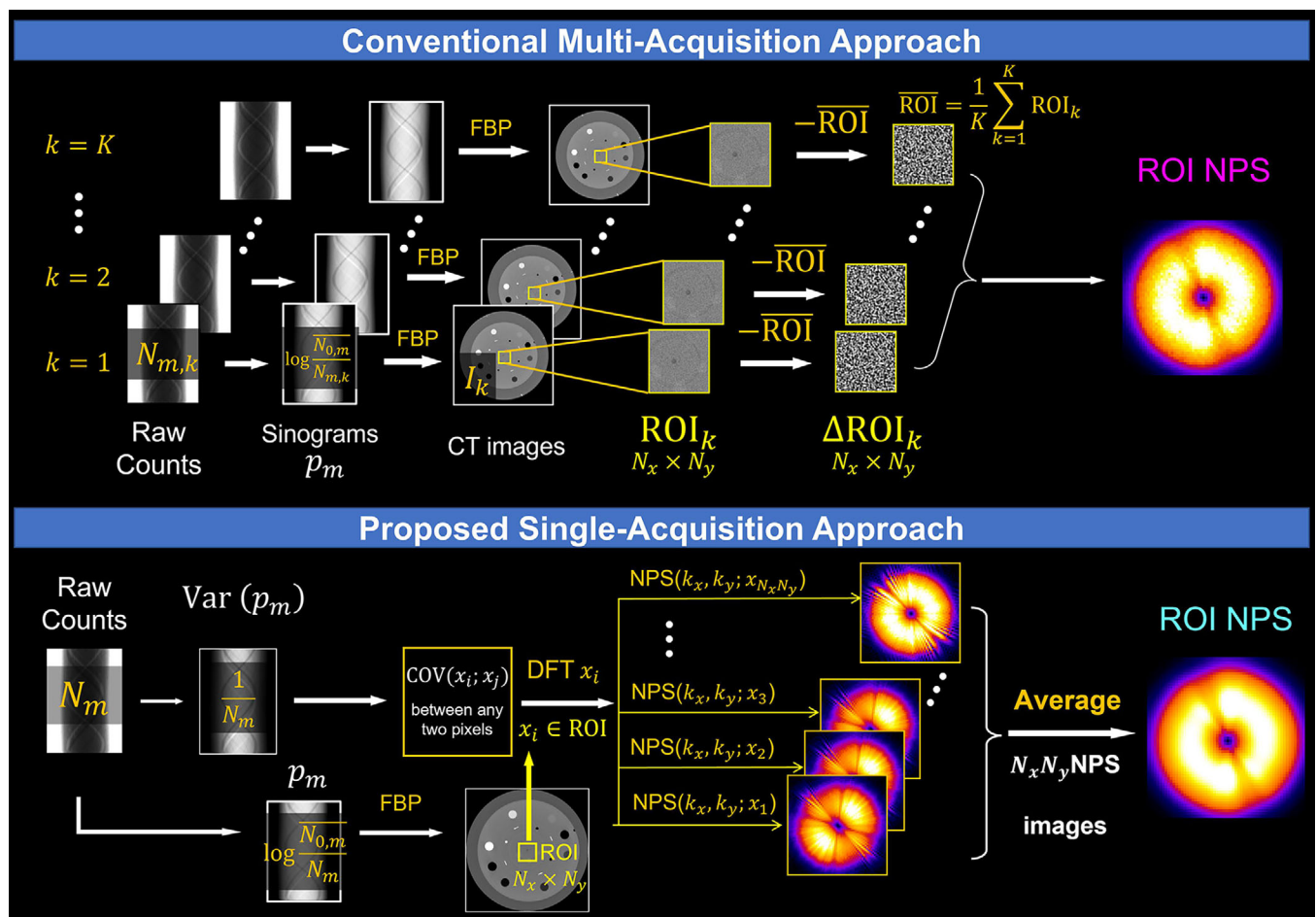


FIGURE 1 (Top row) The workflow of conventional NPS measurement method with K repeated CT acquisitions. (Bottom row) The proposed approach to reconstruct local and task-specific NPS from raw detector counts from a single CT acquisition.

acquisition as described in Section 2.4, raw count data were collected using a benchtop PCD-CT system in the authors' laboratory. This system employs a cadmium telluride (CdTe)-based PCD (model XC-Hydra FX50, manufactured by Varex Imaging, Sweden). The details of the acquisition and image reconstruction parameters are summarized in Table 1.

The experimental studies used three phantoms: (1) a uniform and cylindrical acrylic phantom with a diameter of 16 cm; (2) a Catphan600 phantom (The Phantom Laboratory, Salem, NY), and (3) an anthropomorphic head phantom (Kyoto Kagaku, Japan).

For all PCD-CT scans, the tube potential was fixed at 120 kV. All three phantoms received PCD-CT scans at 240 mAs. To investigate the mAs dependence of the proposed NPS estimation method, additional scans of the 16-cm uniform phantom were performed at 100 kV and each of the following mAs levels: 60, 120, 180, 240, 300, 360, 420, and 480.

To compare the proposed single-acquisition NPS measurement method with the conventional method involving repeated acquisitions, PCD-CT scans of the

TABLE 1 Data acquisition parameters and reconstruction parameters.

Source-to-detector distance	1034.0 mm
Source-to-isocenter distance	571.5 mm
Number of projection views	1200
View angle coverage	2π
Detector coverage	50 cm \times 0.6 cm
Detector pixel size	0.8 mm after binning
Reconstruction algorithm	FBP
Reconstruction pixel size	0.35 mm
Reconstruction image matrix size	512 \times 512
Reconstruction kernel	Ram-Lak
Interpolation scheme	Linear interpolation

16-cm uniform phantom were repeated 100 times at each mAs level. The ROI size is 100 pixels \times 100 pixels. For both the Catphan phantom and the anthropomorphic phantom with heterogeneous structures, data acquisitions were repeated 20 times, and the ROI size was 64 pixels \times 64 pixels.

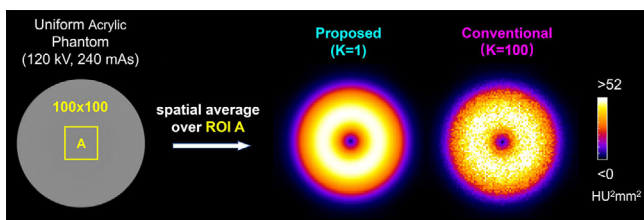


FIGURE 2 Comparisons for NPS measured at a ROI located at the center of the uniform phantom. The proposed NPS method used data from a single PCD-CT scan, while the conventional method used data from 100 repeated scans. NPS, noise power spectra; PCD-CT, photon counting detector-CT; ROI, region of interest.

4 | EXPERIMENTAL RESULTS

In this section, NPS measured using the proposed single-acquisition method and the corresponding results from the conventional method were presented to validate the proposed method.

4.1 | NPS of the uniform acrylic phantom

Figure 2 presents two 2D NPS of the uniform acrylic phantom. One NPS was obtained using the proposed single-acquisition method, averaged over all 100×100 pivotal points within a ROI at the center of the phantom. The other NPS was measured using the conventional method at the same ROI, utilizing data from 100 repeated scans. To facilitate a quantitative comparison of the two 2D NPS in Figure 2, radial profiles of the 2D NPS were evaluated at three angular orientations. As shown in Figure 3, the radial profiles of the two NPS

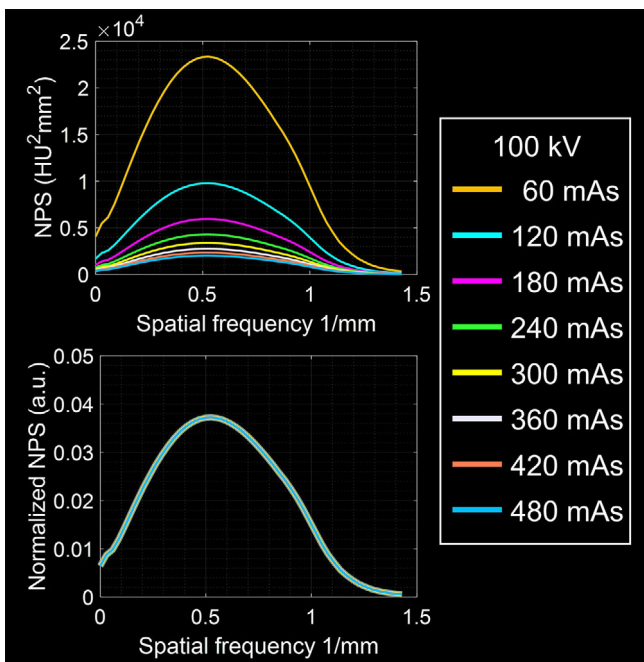


FIGURE 4 Radial profiles of the 2D NPS measured using the proposed method at various mAs levels are depicted. The upper subfigure displays the NPS radial profiles without any normalization, while the lower subfigure presents the normalized NPS radial profiles. The ROI is placed at the center of the uniform phantom. NPS, noise power spectra; ROI, region of interest.

closely align at each of the three angles. However, the proposed method yielded an NPS with higher precision, that is, fewer fluctuations.

In Figure 4, radial profiles of the 2D NPS measured using the proposed method at various mAs levels are

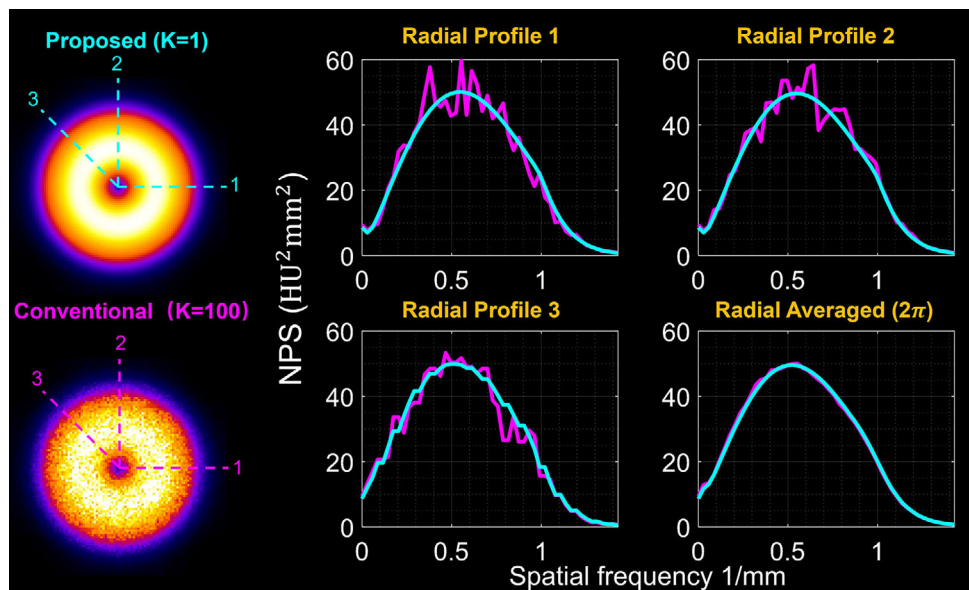


FIGURE 3 Comparison of NPS radial profiles between the proposed method and the conventional method. The radial profiles averaged over all angular directions are shown in the lower right. The ROI is located at the center of the uniform phantom. NPS, noise power spectra; ROI, region of interest.

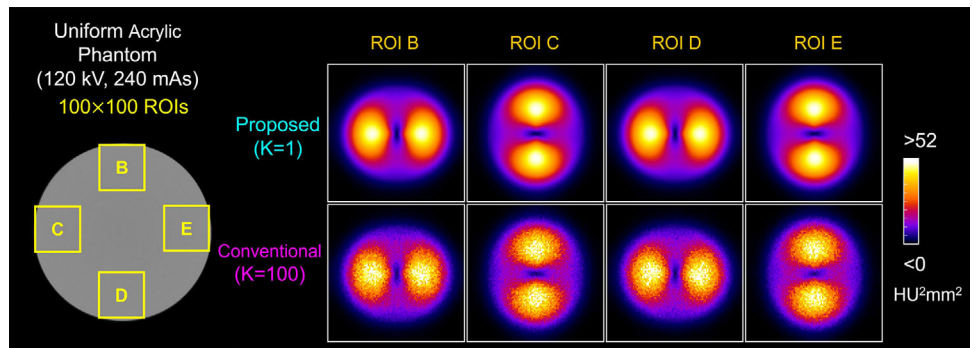


FIGURE 5 2D NPS measured at four different peripheral ROIs in the uniform acrylic phantom. NPS, noise power spectra; ROI, region of interest.

presented. This figure also presents the normalized NPS radial profiles, which are obtained by normalizing the NPS radial profiles with their corresponding area under the curve. The near-perfect overlap of the normalized NPS radial profiles suggests that, for a given PCD-CT system and reconstruction method, the shape of the normalized NPS is largely independent of the mAs level as one would expect.

Finally, the well-known variation of the NPS structure at different spatial locations in a uniform phantom are demonstrated using the proposed NPS measurement method (Figure 5). The results are compared with the NPS measured using the conventional method with 100 acquisitions. The accuracy of the NPS generated using the proposed method, in comparison to the NPS from the conventional method, was quantified by calculating their difference. The corresponding quantitative results are illustrated in Figure 6.

4.2 | NPS of the Catphan phantom

In order to demonstrate the impact of heterogeneity of the image content on the local NPS structures, 2D NPS were measured at nine different ROI locations in the Catphan phantom. Both the proposed ($K = 1$) and the conventional method ($K = 20$) were used.

As shown in Figure 7, due to higher precision of the NPS from the proposed method, the impact of the high contrast inserts and empty holes to the local 2D NPS can be clearly delineated. In contrast, 2D NPS generated using the conventional method has lower precision, even though data from 20 repeated scans were used. The intricate structures within the NPS images from the conventional method, arising from the phantom's heterogeneity, present a challenge in terms of identification. To further quantify the measurement accuracy, a plot depicting the spatial mean difference, that is, the arithmetic average of the intensity values of the difference image within the evaluated ROI, and standard deviation is presented in Figure 8a. It is important to note

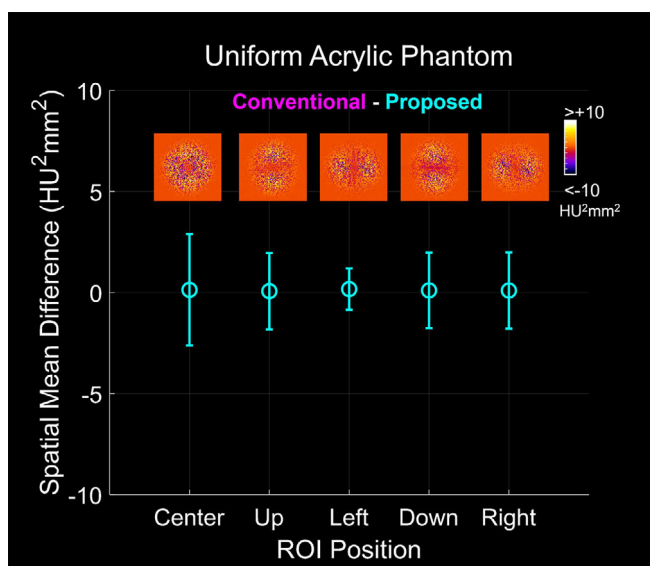


FIGURE 6 Quantitative comparison between the proposed and conventional NPS measurement methods is presented. For each of the four peripheral ROIs depicted in Figure 5, the conventional NPS was subtracted from the proposed NPS. The mean values of these subtraction results are represented by circular markers in the plot, while their standard deviations are depicted as error bars. NPS, noise power spectra; ROI, region of interest.

that the fluctuations observed in the NPS difference image are primarily attributable to fluctuations in the NPS measured using the conventional method.

4.3 | NPS of the anthropomorphic head phantom

To further demonstrate the capability of the proposed method in accurately measuring local NPS in highly heterogeneous objects with a single acquisition, two nylon rods were attached to the surface of the anthropomorphic phantom prior to the PCD-CT scan. This was performed to emulate potential confounding factors encountered in patient exams, such as dangling wires

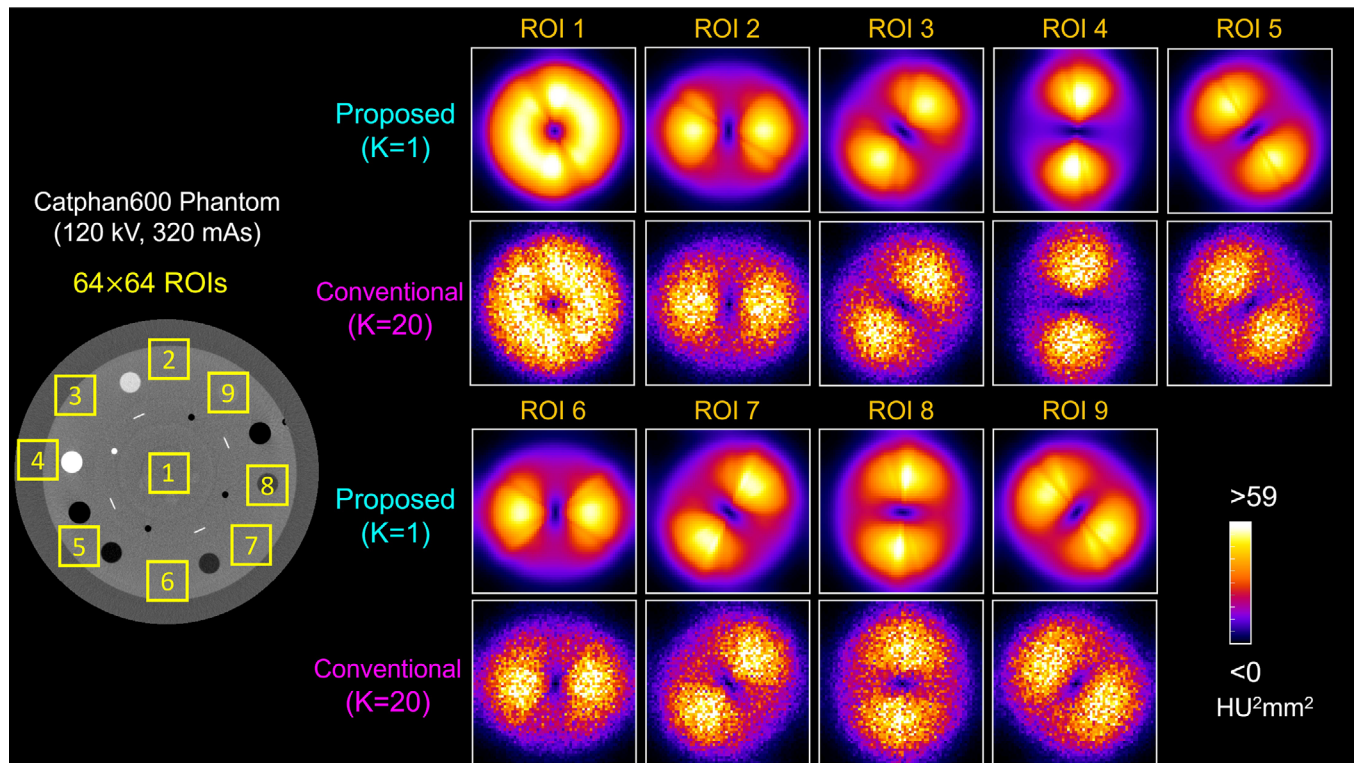


FIGURE 7 2D NPS were measured at nine ROIs in the PCD-CT images of a Catphan600 phantom. For the conventional NPS measurement methods, $K = 20$. NPS, noise power spectra; PCD-CT, photon counting detector-CT; ROI, region of interest.

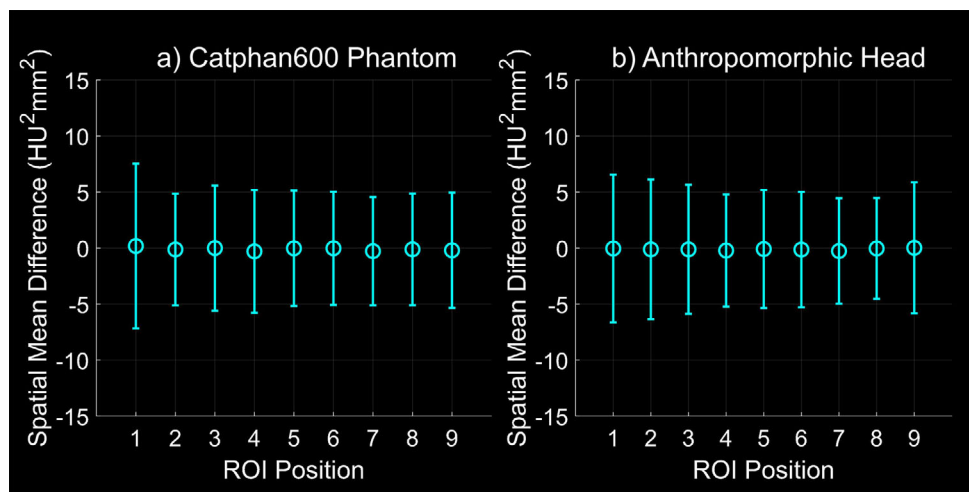


FIGURE 8 Quantitative analysis of the differences between the noise power spectra (NPS) obtained using the proposed method and those obtained using the conventional method. (a) Analysis results for the Catphan600 Phantom. (b) Analysis results for the anthropomorphic head phantom. For each phantom, quantitative analyses were performed at nine regions of interest (ROIs). Both the spatial mean and standard deviation are presented, with units in $\text{HU}^2 \text{mm}^2$.

or IV lines in clinical practice. 2D local NPS results measured with this object are shown in Figure 9. Results of quantitative comparison between the proposed and conventional NPS measurement methods are presented in Figure 8b. The mean differences of nearly zero indicate that the proposed local NPS measurement from single PCD-CT acquisitions is accurate while, as men-

tioned before, the large measurement error bars in the differences are largely due to the higher fluctuations in the measured NPS from the conventional method. These results clearly demonstrate that the proposed NPS measurement method opens the door to local NPS measurements in clinical setting since it only needs one single PCD-CT acquisition.

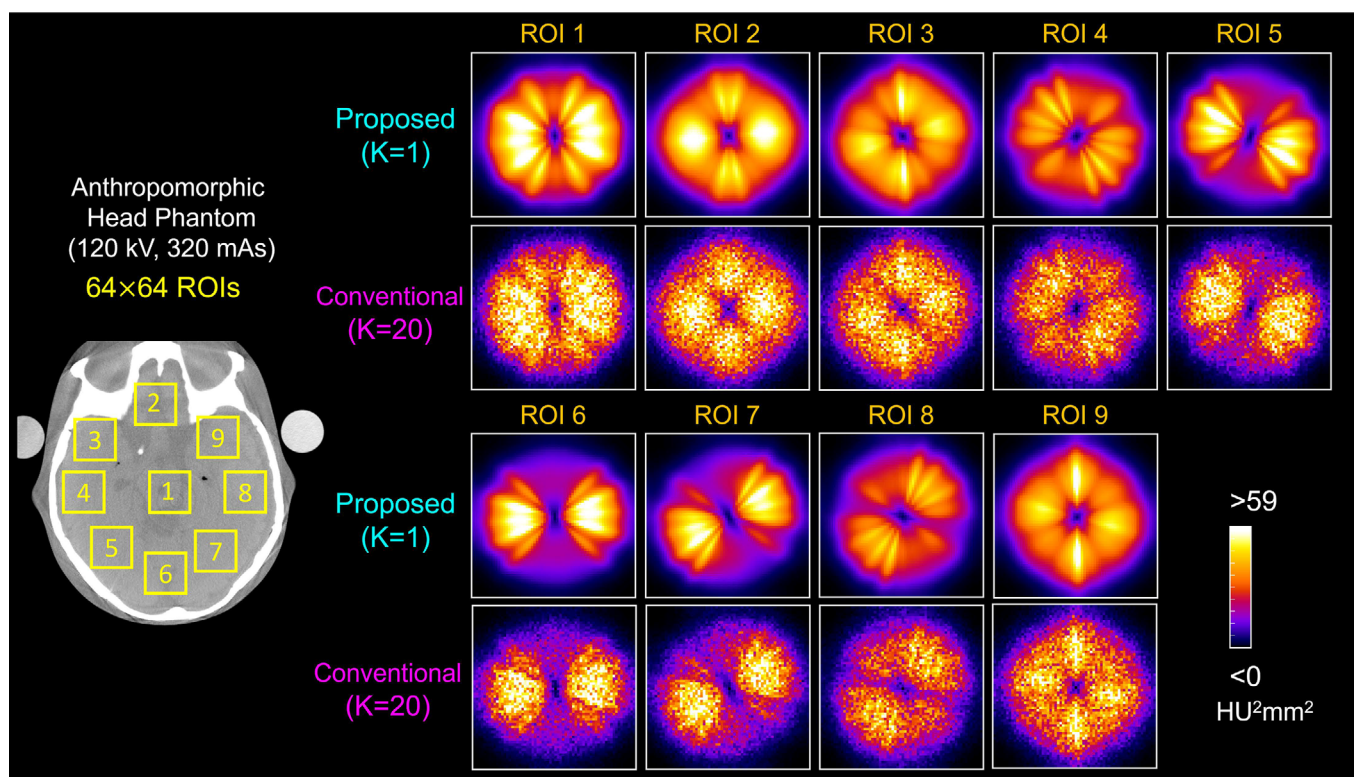


FIGURE 9 2D NPS measured at nine ROI locations in the PCD-CT images of an anthropomorphic head phantom. For the conventional NPS measurement methods, $K = 20$. NPS, noise power spectra; PCD-CT, photon counting detector-CT; ROI, region of interest.

5 | DISCUSSION

In this work, a new method to enable NPS measurement from a single PCD-CT acquisition ($K = 1$) was developed and validated by comparing the measurement results with the conventional method with repeated acquisitions ($K = 100$ for uniform acrylic phantom and $K = 20$ for the two heterogeneous phantoms). The workflow of the proposed single acquisition-based NPS measurement method is summarized as follows:

1. Raw counts N_m is acquired via a single PCD-CT acquisition.
2. The log-transformed projection data \hat{p}_m is computed.
3. The PCD-CT image is reconstructed using an appropriate reconstruction algorithm.
4. For each PCD-CT image pixel/voxel at \vec{x}_i , the variance $\widehat{\sigma}_i^2(\vec{x}_i)$ is computed using Equation (16).
5. For each pair of PCD-CT image pixels \vec{x}_i and \vec{x}_j , the covariance $\widehat{\text{COV}}_i(\vec{x}_i; \vec{x}_j)$ is computed using Equation (15).
6. For a ROI centered around a pivotal point \vec{x}_i , the local 2D NPS, that is, $\widetilde{\text{NPS}}(k_x, k_y; \vec{x}_i)$ is computed using Equation (17).
7. If one is interested in the overall NPS for a given ROI, namely $\overline{\text{NPS}}_{\text{ROI}}(k_x, k_y)$, it can be computed using Equation (18).

By following the above workflow, local NPS can be obtained using data from a single PCD-CT acquisition.

As is widely recognized, the NPS is a vital component of task-specific quantitative image quality assessment.⁴⁴ For a specific diagnostic imaging task, the quantitative image quality can be evaluated using metrics such as the lesion detectability index (d'^2) within a validated observer model. In these mathematical observer models, it is essential to rely on the locally measured NPS and the MTF at the lesion's location to provide a clinically relevant estimation of how imaging performance might vary with imaging parameters such as radiation exposure level and scanning protocols. In the context of this quantitative image quality assessment, the NPS estimation method introduced in this study, which has been validated through phantom studies, represents a significant advance for patient-specific and localized NPS measurements in Photon Counting Detector CT (PCD-CT). It meets two crucial criteria: first, it enables the measurement of NPS without exposing the patient to the repeated radiation typical of CT exams; second, it permits the selection of a ROI for local NPS calculation that is tailored to the patient's anatomy, thus avoiding the need for a large, uniform square ROI. The implications of utilizing local NPS measurement in this research will be explored further in future studies.

There are several limitations in this work as well. First, although it has been experimentally demonstrated that

the proposed method with a single set of PCD-CT data provides a more precise estimation of the local NPS than the conventional method with repeated acquisitions, no theoretical analysis is presented to explain the underlining reason. This limitation will be addressed in a separate paper where the missing theoretical analysis and further generalization of the results will be presented. Second, the proposed method is only applicable to PCD-CT. For energy integrating detector-CT (EID-CT) systems, the digital outputs of the detector do not necessarily follow the Poisson distribution, and thus the validity of the projection variance estimator in Equation (10) is uncertain. Additional modifications are needed to generalize the proposed method to EID-CTs. Third, the proposed method requires access to raw detector counts, which may not be available to end users. Further technical developments are needed to enable single acquired-based NPS measurement when the raw count data are unavailable. Fourth, when radiation exposure levels are low, there can be some minor statistical biases in the projection variance estimator presented in Equation (10). In those cases, it may be advantageous to utilize the higher-order estimator presented in Equation (14) for the projection variance when calculating local NPS from a single PCD-CT data acquisition. Finally, it remains an open question how to apply the method presented in this work to other nonlinear reconstruction methods, such as model-based statistical image reconstruction methods or the recently introduced data-driven, deep learning-based methods. For the linear FBP reconstruction method, the noise covariance matrix can be reconstructed from the constructed noise variance estimator of the projection data due to its linearity. However, it is not yet clear how to reconstruct the noise covariance matrix from the estimated noise variance of the projection data when using nonlinear image reconstruction methods.

6 | CONCLUSION

A new method to estimate PCD-CT NPS from a single data acquisition has been developed and experimentally validated. The proposed method enables PCD-CT image covariance and NPS to be estimated without performing repeated scans. This method provides a more efficient approach to quantify PCD-CT image quality, which is crucial for optimizing or evaluating PCD-CT systems, scan protocols, and reconstruction algorithms.

ACKNOWLEDGMENTS

This work is partially supported by NIH through Grants R01EB034011, R01EB032474, and R01HL153594. The work is also partially supported by GE Healthcare. One of the authors, G.H.C., received partial support from the WARF Named Professorship, a chaired professorship bestowed by the University of Wisconsin—Madison's

Office of the Vice Chancellor for Research and Graduate Education, with funding from the Wisconsin Alumni Research Foundation (WARF).

CONFLICT OF INTEREST STATEMENT

The authors declare no conflicts of interest.

REFERENCES

1. Mandel L. Image fluctuations in cascade intensifiers. *Br J Appl Phys.* 1959;10:233.
2. Riederer SJ, Pelc NJ, Chesler DA,. The noise power spectrum in computed X-ray tomography. *Phys Med Biol.* 1978;23:446-454.
3. Faulkner K, Moores B. Analysis of x-ray computed tomography images using the noise power spectrum and autocorrelation function. *Phys Med Biol.* 1984;29:1343-1352.
4. Giger ML, Doi K, Metz CE. Investigation of basic imaging properties in digital radiography. 2. Noise Wiener spectrum. *Med Phys.* 1984;11:797-805.
5. Tapiolaara MJ, Wagner R. SNR and DQE analysis of broad spectrum x-ray imaging. *Phys Med Biol.* 1985;30:519.
6. Rabbani M, Shaw R, Van Metter R. Detective quantum efficiency of imaging systems with amplifying and scattering mechanisms. *JOSA A.* 1987;4:895-901.
7. Wilson DW, Tsui BM. Noise properties of filtered-backprojection and ML-EM reconstructed emission tomographic images. *IEEE Trans Nucl Sci.* 1993;40:1198-1203.
8. Siewersden JH, Antonuk LE, El-Mohri Y, Yorkston J, Huang W, Boudry JM, Cunningham IA. Empirical and theoretical investigation of the noise performance of indirect detection, active matrix flat-panel imagers (AMFPIS) for diagnostic radiology. *Med Phys.* 1997;24:71-89.
9. Siewersden J, Cunningham I, Jaffray D. A framework for noise-power spectrum analysis of multidimensional images. *Med Phys.* 2002;29:2655-2671.
10. Pan X, Yu L. Image reconstruction with shift-variant filtration and its implication for noise and resolution properties in fan-beam computed tomography. *Med Phys.* 2003;30:590-600.
11. Zeng GL. Nonuniform noise propagation by using the ramp filter in fan-beam computed tomography. *IEEE Trans Med Imaging.* 2004;23:690-695.
12. Boedecker KL, Cooper VN, McNitt-Gray MF. Application of the noise power spectrum in modern diagnostic MDCT: part I. Measurement of noise power spectra and noise equivalent quanta. *Phys Med Biol.* 2007;52:4027-4046.
13. Boedecker K, McNitt-Gray M. Application of the noise power spectrum in modern diagnostic MDCT: part II. Noise power spectra and signal to noise. *Phys Med Biol.* 2007;52:4047.
14. Wunderlich A, Noo F. Image covariance and lesion detectability in direct fan-beam x-ray computed tomography. *Phys Med Biol.* 2008;53:2471-2493.
15. Yang Kai, Kwan ALC, Huang S-Y, Packard NJ, Boone, JM,. Noise power properties of a cone-beam CT system for breast cancer detection. *Med Phys.* 2008;35:5317-5327.
16. Tward DJ, Siewersden JH. Cascaded systems analysis of the 3D noise transfer characteristics of flat-panel cone-beam CT. *Med Phys.* 2008;35:5510-5529.
17. Tward DJ, Siewersden JH. Noise aliasing and the 3D NEQ of flat-panel cone-beam CT: Effect of 2D/3D apertures and sampling. *Med Phys.* 2009;36:3830-3843.
18. Baek J, Pelc NJ. The noise power spectrum in CT with direct fan beam reconstruction. *Med Phys.* 2010;37:2074-2081.
19. Baek J, Pelc NJ. Local and global 3D noise power spectrum in cone-beam CT system with FDK reconstruction. *Med Phys.* 2011;38:2122-2131.
20. Baek J, Pelc NJ. Effect of detector lag on CT noise power spectra. *Med Phys.* 2011;38:2995-3005.

21. Pal D, Kulkarni S, Yadava G, Thibault B, Sauer K, Hsieh J. Analysis of noise power spectrum for linear and non-linear reconstruction algorithms for CT. In: 2011 IEEE Nuclear Science Symposium Conference Record. IEEE; 2011:4382-4385.
22. Zeng R, Petrick N, Gavrielides MA, Myers KJ. Approximations of noise covariance in multi-slice helical CT scans: impact on lung nodule size estimation. *Phys Med Biol*. 2011;56:6223.
23. IEC. Medical electrical equipment-characteristics of digital X-ray imaging devices – part 1-1: determination of the detective quantum efficiency – detectors used in radiographic imaging. IEC 62220-1-1. International Electrotechnical Commission; 2015.
24. International Commission on Radiation Units and Measurements. ICRU report no. 87: Radiation dose and image-quality assessment in computed tomography. *J ICRU*. 2012;12:1-149.
25. Pineda AR, Tward DJ, Gonzalez A, Siewerdsen JH. Beyond noise power in 3D computed tomography: the local NPS and off-diagonal elements of the Fourier domain covariance matrix. *Med Phys*. 2012;39:3240-3252.
26. Solomon J, Samei E. Quantum noise properties of CT images with anatomical textured backgrounds across reconstruction algorithms: FBP and SAFIRE. *Med Phys*. 2014;41:091908.
27. Li K, Tang J, Chen G-H. Statistical model based iterative reconstruction (MBIR) in clinical CT systems: experimental assessment of noise performance. *Med Phys*. 2014;41:041906.
28. Lauzier PT, Chen G-H. Characterization of statistical prior image constrained compressed sensing. I. Applications to time-resolved contrast-enhanced CT. *Med Phys*. 2012;39:5930-5948.
29. Lauzier PT, Tang J, Chen G-H. Prior image constrained compressed sensing: implementation and performance evaluation. *Med Phys*. 2012;39:66-80.
30. Friedman SN, Fung GS, Siewerdsen JH, Tsui BM. A simple approach to measure computed tomography (CT) modulation transfer function (MTF) and noise-power spectrum (NPS) using the American College of Radiology (ACR) accreditation phantom. *Med Phys*. 2013;40:051907.
31. Melnyk R, Boudry J, Liu X, Adamak M. Anti-scatter grid evaluation for wide-cone CT. In: *Medical Imaging 2014: Physics of Medical Imaging*. Vol 9033. SPIE; 2014:778-784.
32. Gomez-Cardona D, Li K, Lubner MG, Pickhardt PJ, Chen G-H. Noise performance studies of model-based iterative reconstruction (MBIR) as a function of kV, mA and exposure level: impact on radiation dose reduction and image quality. In: *Medical Imaging 2015: Physics of Medical Imaging*. Vol 9412. SPIE; 2015:801-807.
33. Zeng R, Gavrielides MA, Petrick N, Sahiner B, Li Q, Myers KJ. Estimating local noise power spectrum from a few FBP-reconstructed CT scans. *Med Phys*. 2016;43:568-582.
34. Schmitt SM, Goodsitt MM, Fessler JA. Fast variance prediction for iteratively reconstructed CT images with locally quadratic regularization. *IEEE Trans Med Imaging*. 2016;36:17-26.
35. Gomez-Cardona D, Li K, Hsieh J, Lubner MG, Pickhardt PJ, Chen G-H. Can conclusions drawn from phantom-based image noise assessments be generalized to in vivo studies for the nonlinear model-based iterative reconstruction method? *Med Phys*. 2016;43:687-695.
36. Gomez-Cardona D, Cruz-Bastida JP, Li K, Budde A, Hsieh J, Chen G-H. Impact of bowtie filter and object position on the two-dimensional noise power spectrum of a clinical MDCT system. *Med Phys*. 2016;43:4495-4506.
37. Cruz-Bastida JP, Gomez-Cardona D, Garrett J, Szczykutowicz T, Chen G-H, Li K. Modified ideal observer model (MIOM) for high-contrast and high-spatial resolution CT imaging tasks. *Med Phys*. 2017;44:4496-4505.
38. Hayes J, Gomez-Cardona D, Garrett J, Zhang R, Chen G-H. Noise and spatial resolution characteristics of unregularized statistical iterative reconstruction: an experimental phantom study. In: *Medical Imaging 2018: Physics of Medical Imaging*. Vol 10573. SPIE; 2018:777-783.
39. Li K, Chen G-H. CT image quality characterization. In: Samei E, Pelc NJ (eds.), *Computed Tomography*. Springer; 2020:85-124.
40. Nickoloff EL, Riley R. A simplified approach for modulation transfer function determinations in computed tomography. *Med Phys*. 1985;12:437-442.
41. Richard S, Husarik DB, Yadava G, Murphy SN, Samei E. Towards task-based assessment of CT performance: system and object MTF across different reconstruction algorithms. *Med Phys*. 2012;39:4115-4122.
42. Li K, Garrett J, Ge Y, Chen G-H. Statistical model based iterative reconstruction (MBIR) in clinical CT systems. Part II. Experimental assessment of spatial resolution performance. *Med Phys*. 2014;41:071911.
43. Cruz-Bastida JP, Gomez-Cardona D, Li K, et al. Hi-Res scan mode in clinical MDCT systems: experimental assessment of spatial resolution performance. *Med Phys*. 2016;43:2399-2409.
44. Barrett HH, Myers KJ. *Foundations of Image Science*. John Wiley & Sons; 2013.
45. Hanson KM. Detectability in computed tomographic images. *Med Phys*. 1979;6:441-451.
46. Myers KJ, Barrett HH. Addition of a channel mechanism to the ideal-observer model. *JOSA A*. 1987;4:2447-2457.
47. Burgess AE, Jacobson FL, Judy PF. Human observer detection experiments with mammograms and power-law noise. *Med Phys*. 2001;28:419-437.
48. Abbey CK, Barrett HH. Human-and model-observer performance in ramp-spectrum noise: effects of regularization and object variability. *JOSA A*. 2001;18:473-488.
49. Gang GJ, Lee J, Stayman JW, Tward DJ, Zbijewski W, Prince JL, Siewerdsen JH. Analysis of Fourier-domain task-based detectability index in tomosynthesis and cone-beam CT in relation to human observer performance. *Med Phys*. 2011;38:1754-1768.
50. Yu L, Leng S, Chen L, Kofler JM, Carter RE, McCollough CH. Prediction of human observer performance in a 2-alternative forced choice low-contrast detection task using channelized Hotelling observer: impact of radiation dose and reconstruction algorithms. *Med Phys*. 2013;40:041908.
51. Leng S, Yu L, Zhang Y, Carter R, Toledano AY, McCollough CH. Correlation between model observer and human observer performance in CT imaging when lesion location is uncertain. *Med Phys*. 2013;40:081908.
52. Li K, Garrett J, Chen G-H. Correlation between human observer performance and model observer performance in differential phase contrast CT. *Med Phys*. 2013;40:111905.
53. Gang GJ, Stayman JW, Zbijewski W, Siewerdsen JH. Task-based detectability in CT image reconstruction by filtered backprojection and penalized likelihood estimation. *Med Phys*. 2014;41:081902.
54. Solomon JB, Samei E. Correlation between human detection accuracy and observer model-based image quality metrics in computed tomography. *J Med Imaging*. 2016;3:035506.
55. Chen JR, Feng M, Li K. Overcoming the challenges of inaccurate CT numbers in low dose CT. *Proc SPIE*. 2022;12031:276-281.
56. Li K, Chen JR, Feng M. Construction of a nearly unbiased statistical estimator of sinogram to address CT number bias issues in low-dose photon counting CT. *IEEE Trans Med Imag*. 2023;42:1846-1858.
57. Bushe D, Zhang R, Chen G-H, Li K. Unbiased zero-count correction method in low-dose high-resolution photon counting detector CT. *Phys Med Biol*. 2023;68:115002.
58. Griner D, Lei N, Chen G-H, Li K. Correcting statistical CT number biases without access to raw detector counts: applications to high spatial resolution photon counting CT imaging. *Med Phys*. 2023;50:6022-6035.

How to cite this article: Zhang C, Li K, Zhang R, Chen G-H. Experimental measurement of local noise power spectrum (NPS) in photon counting detector-CT (PCD-CT) using a single data acquisition. *Med Phys.* 2024;51:4081–4094. <https://doi.org/10.1002/mp.17110>

APPENDIX A: CONCISE NOTATION OF FBP IMAGE RECONSTRUCTION

Given the linearity of the filtered backprojection (FBP) reconstruction, it follows that the reconstructed image at a point \vec{x} is a certain combination of the measured line integral projection data. For a concrete and precise understanding of this concept, it is crucial to elucidate how the coefficients $\lambda_m(\vec{x})$ integrate other reconstruction details into a simplified form. This appendix presents detailed derivations to clarify these elements, thereby facilitating numerical implementations.

The fan beam data acquisition geometry employing a flat-panel detector and its corresponding geometrical factors are illustrated in Figure A1. Using this geometry, the image value $f(\vec{x})$ for a given point \vec{x} within the field of view is given by the standard filtered backprojection formula from the sinogram data $y(u, t)$:

$$I(\vec{x}) = \int_0^{\Gamma} dt w_r(z(\vec{x}, t), t) w_b(\vec{x}, t) [w_g(u)y(u, t)] \\ \otimes h_{\text{ramp}}(u) |_{u=z(\vec{x}, t)}, \quad (\text{A1})$$

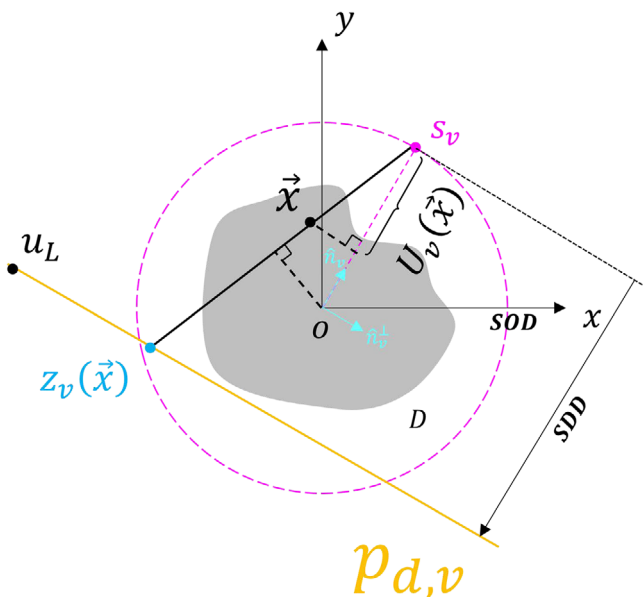


FIGURE A1 The geometry of CT acquisition and backprojection scheme.

where h_{ramp} is the ramp kernel, and $w_r(u, t)$ is the weighting factor that compensates for redundant data. The factors $w_b(u, t)$ and $w_g(u)$ in Equation (A1) are defined as

$$w_b(u, t) = \frac{\text{SDD} \cdot \text{SOD}}{U^2(\vec{x}, t)},$$

$$w_g(u) = \frac{\text{SDD}}{\sqrt{\text{SDD}^2 + u^2}},$$

where SDD denotes the source-to-detector distance, and SOD is the source-to-iso distance. Figure A1 depicts the geometrical interpretation of the factor $U(\vec{x}, t)$.

To numerically reconstruct the image value at a point \vec{x} within the FOV, the FBP reconstruction shown in Equation (A1) can be rewritten as a discrete summation of contributions from individual detector elements, labeled by the index $d \in D$ at a view angle indexed by $v \in V$. Here, V and D represent the total number of view angles and total detector elements at each view angle, respectively. Δv labels the view angle sampling interval, and Δu labels the detector pixel size.

With these notations, the FBP form depicted in Equation (2) in the main text of the paper can be derived through the following steps.

- Step 1: Geometric weighting. According to Equation (A1), the projection data are first weighted by a geometric factor w_d , that is,

$$p_{d,v}^w = w_d p_{d,v}$$

- Step 2: Filtering. Then the weighted projection data is filtered by the digital ramp kernel h_d as follows:

$$\tilde{p}_{d',v} = \Delta u \sum_d h_{D-d'+d} \cdot p_{d,v}^w$$

- Step 3: Determine which detector pixels to backproject. Let us consider one view angle only at view angle v . At this view angle, the x-ray going through the image point \vec{x} will hit the detector at index $z_v(\vec{x}) \in \mathbb{R}$:

$$z_v(\vec{x}) = \text{SDD} \frac{\vec{x} \cdot \hat{n}_v^\perp}{\text{SOD} - \vec{x} \cdot \hat{n}_v}$$

which is the coordinate in between two detector elements. The index of the two adjacent elements are

$$d'_L = d'_v(\vec{x}) = \left\lfloor \frac{z_v(\vec{x}) - u_L}{\Delta u} \right\rfloor;$$

$$d'_R = d'_v(\vec{x}) + 1 = \left\lfloor \frac{z_v(\vec{x}) - u_L}{\Delta u} \right\rfloor + 1.$$

where $\lfloor \cdot \rfloor$ is the floor operation and the u_L is the coordinate for the left-most detector element. It is

transparent that under this view angle, only the two detector pixels can contribute to the reconstructed image $\hat{I}(\vec{x})$.

- Step 4: Interpolation. Their contribution is further split by the interpolation process, the weighting factor $\alpha_v(\vec{x})$ can be determined by linear interpolation scheme, that is,

$$\alpha_v(\vec{x}) = \frac{z_v(\vec{x}) - u_L}{\Delta u} - d'.$$

For simplicity and without loss of generality, nearest neighbor linear interpolation was used to interpolate data from the left and the right nearest detectors:

$$\begin{aligned}\tilde{p}_v^L(\vec{x}) &= [1 - \alpha_v(\vec{x})]\tilde{p}_{d'_L, v} \\ &= \Delta u[1 - \alpha_v(\vec{x})] \sum_d [h_{D-d'_L+d}] w_d p_{d, v}, \\ \tilde{p}_v^R(\vec{x}) &= [\alpha_v(\vec{x})]\tilde{p}_{d'_R, v} = \Delta u[\alpha_v(\vec{x})] \sum_d [h_{D-d'_R+d}] w_d p_{d, v}.\end{aligned}$$

- Step 5: Redundancy weighting. This step can be misinterpreted. In our work, the weighting scheme is the parker weighting scheme denoted as $\eta_{d', v}$ for $\tilde{p}_{d', v}$. It is straightforward to perform such weighting

$$\begin{aligned}\tilde{P}_v^{\text{Parker}}(\vec{x}) &= [\eta_{d'_L, v}]\tilde{p}_v^L(\vec{x}) + [\eta_{d'_R, v}]\tilde{p}_v^R(\vec{x}), \\ &= \Delta u[\eta_{d'_v(\vec{x}), v}][1 - \alpha_v(\vec{x})] \sum_d [h_{D-d'_v(\vec{x})+d}] w_d p_{d, v} \\ &\quad + \Delta u[\eta_{d'_v(\vec{x})+1, v}][\alpha_v(\vec{x})] \sum_d [h_{D-(d'_v(\vec{x})+1)+d}] w_d p_{d, v}.\end{aligned}$$

- Step 6: Weighted backprojection. In this step, the backprojection weighting only concerns the view angle.

$$\hat{I}_v(\vec{x}) = b_v(\vec{x})\tilde{P}_v^{\text{Parker}}(\vec{x}),$$

where $b_v(\vec{x}) = \frac{\text{SOD-SDD}}{U_v^2(\vec{x})}$ and $U_v(\vec{x}) = \text{SOD} - \vec{x} \cdot \hat{n}_v$.

The backprojection scheme can be referred to Figure A1.

- Sum all view angles.

$$\hat{I}(\vec{x}) = \sum_v \Delta v \hat{I}_v(\vec{x}) = \sum_v \Delta v b_v(\vec{x}) \tilde{P}_v^{\text{Parker}}(\vec{x})$$

The final form of the structured FBP equation can be presented in summation form:

$$\hat{I}(\vec{x}) = \sum_{d, v} \lambda_{d, v}(\vec{x}) p_{d, v}, \quad (\text{A2})$$

where $\lambda_{d, v}(\vec{x})$ is given as below:

$$\begin{aligned}\lambda_{d, v}(\vec{x}) &= [\Delta u \Delta v] b_v(\vec{x}) w_d \left[[\eta_{d'_v(\vec{x}), v}][1 - \alpha_v(\vec{x})][h_{D-d'_v(\vec{x})+d}] \right. \\ &\quad \left. + [\eta_{d'_v(\vec{x})+1, v}][\alpha_v(\vec{x})][h_{D-(d'_v(\vec{x})+1)+d}] \right].\end{aligned}$$

To further simplify the notation, we introduce a single index $m = (d, v)$, which represents both the detector and view angle indices. This notation allows us to attain the linear form as depicted in Equation (2) in the main body of the paper from Equation (A2).

APPENDIX B: CONSTRUCTION OF HIGHER-ORDER APPROXIMATIONS OF THE STATISTICAL ESTIMATOR OF VARIANCE OF PROJECTION DATA

Consider a Poisson variable N_m with mean parameter \bar{N}_m . This appendix outlines the construction of a nearly bias-free estimator and the determination of coefficients for higher-order terms in its expansion. The expectations $E\left(\frac{1}{N_m^k}\right)$ for $k = 1, 2, 3$ can be readily calculated to obtain the following results:

$$E\left(\frac{1}{N_m}\right) = \frac{1}{\bar{N}_m} + \frac{1}{\bar{N}_m^2} + \frac{1}{2\bar{N}_m^3} + O\left(\frac{1}{\bar{N}_m^4}\right), \quad (\text{B1})$$

$$E\left(\frac{1}{N_m^2}\right) = \frac{1}{\bar{N}_m^2} + \frac{1}{2\bar{N}_m^3} + O\left(\frac{1}{\bar{N}_m^4}\right), \quad (\text{B2})$$

$$E\left(\frac{1}{N_m^3}\right) = \frac{1}{\bar{N}_m^3} + O\left(\frac{1}{\bar{N}_m^4}\right). \quad (\text{B3})$$

These results can now be employed to construct a nearly bias-free estimator for projection variance estimation. Up to the third order, we propose an estimator of the form:

$$\widehat{\text{var}}(\hat{p}_m)^{\text{bias-free}} = \frac{1}{N_m} + \frac{a}{N_m^2} + \frac{b}{N_m^3}, \quad (\text{B4})$$

where a and b are real numbers to be determined. Our goal is to determine the coefficients a and b such that the expectation of the estimator matches the series expansion up to $O\left(\frac{1}{\bar{N}_m^4}\right)$. Specifically, we require

$$\begin{aligned}E\left(\frac{1}{N_m} + \frac{a}{N_m^2} + \frac{b}{N_m^3}\right) &= \text{Var}(\hat{p}_m) = \frac{1}{\bar{N}_m} + \frac{3}{2\bar{N}_m^2} \\ &\quad + \frac{43}{12\bar{N}_m^3} + O\left(\frac{1}{\bar{N}_m^4}\right). \quad (\text{B5})\end{aligned}$$

Upon solving the above equation, we find the coefficients to be

$$a = \frac{1}{2}, \quad b = \frac{1}{12}. \quad (\text{B6})$$

These values ensure that our estimator is nearly bias-free up to the third order of \bar{N}_m . The final constructed

estimator is

$$\widehat{\text{var}(\hat{p}_m)}^{\text{bias-free}} = \frac{1}{N_m} + \frac{1}{2N_m^2} + \frac{1}{12N_m^3}, \quad (\text{B7})$$

which is the same as Equation (14).

To aid readers in understanding the foundational principles behind our construction, we intend to clarify the rationale before finalizing this appendix. At first glance, the method might seem paradoxical, as it involves adding extra terms with statistical biases to generate an estimator with diminished statistical bias. Yet, upon reflecting on a crucial observation—that the statistical

bias of the random variable $1/N^k$ (with N following a Poisson distribution) escalates to a higher order—the strategy becomes clear. It is evident that there is an opportunity to reduce the statistical bias by developing a superior estimator through linear combinations of higher-order terms $\frac{a_k}{N^k}$. By carefully choosing the combination coefficients a_k , we can engineer these higher-order biases, which stem from aggregated terms in the form $1/N^k$, to cancel each other out effectively. This method has been rigorously explored in our previous studies, especially in efforts to rectify CT number bias.^{55–58}